Pure appl. geophys. 161 (2004) 2139–2153
0033 – 4553/04/122139 – 15
DOI 10.1007/s00024-004-2554-x

© Birkhäuser Verlag, Basel, 2004

Pure and Applied Geophysics

# On the Effects of Non-planar Geometry for Blind Thrust Faults on Strong Ground Motion

HIDEO AOCHI[1,2] and KIM B. OLSEN[1]

*Abstract* — We quantify the effects of complex fault geometry on low-frequency (< 1 Hz) strong ground motion using numerical modeling of dynamic rupture. Our tests include the computation of synthetic seismograms for several simple rupture scenarios with planar and curved fault approximations of the 1994 Northridge earthquake. We use the boundary integral equation method (BIEM) to compute the dynamic rupture process, which includes the normal stress effects along the curved fault geometries. The wave propagation and computation of synthetic seismograms are modeled using a fourth-order finite-difference method (FDM). The near-field ground motion is significantly affected by the acceleration, deceleration and arrest of rupture due to the curvature of the faults, as well as the variation in directivity of the rupture. For example, a 6-km-long hanging-wall or footwall splay with a maximum offset of 1 km can change 1-Hz peak velocities by up to a factor of 2-3 near the fault. Our tests suggest that the differences in waveform are larger on the hanging wall compared to those on the footwall, although the differences in amplitude are larger in the forward rupture direction (footwall). The results imply that kinematic ground motion estimates may be biased by the omission of dynamic rupture effects and even relatively gentle variation in fault geometry, and even for long-period waves.

**Key words:** Non-planar geometry, blind thrust fault, strong gound motion, dynamic rupture propagation, boundary integral equation method, and finite-difference method.

## *Introduction*

Geologists have pointed out for decades that complex fault geometry plays a significant role in the initiation, propagation and healing of earthquakes (e.g., KING and NÁBĚLEK, 1985; SIBSON, 1986). Furthermore, a series of studies have examined this problem both theoretically and numerically, supporting the field results. For example, HARRIS and DAY (1993, 1999) and KASE and KUGE (1998) investigated spontaneous rupture processes between parallel or perpendicular orientations of fault segments in 2-D or 3-D media. Rupture processes for even more complex fault or crack orientation were modeled by TADA and YAMASHITA (1996, 1997) and KAME and YAMASHITA (1997, 1999) in 2-D media, and AOCHI *et al.* (2000a,b, 2002), OGLESBY *et al.* (2001) and OGLESBY and ARCHULETA (2003) in 3-D media.

[1]Institute for Crustal Studies, UC Santa Barbara, Santa Barbara, CA 93106, USA.
E-mail: kbolsen@crustal.ucsb.edu
[2]H. A. is now at the Institut de Radioprotection et de Sûreté Nucléaire (IRSN), France.

Many of the modeling studies mentioned above considered strike-slip faults with surface rupture, which can be most easily observed in the field. However, recent studies using reflection seismology have shown that it is possible to estimate detailed geometry of buried dipping faults. It is numerically complicated to correctly model the dynamic effects of a fault dipping with respect to the free surface, even for a planar fault geometry. MIKUMO and MIYATAKE (1993) and NIELSEN and OLSEN (2000) used finite-difference methods with a stretched grid and a stair-step approximation of the free-surface boundary condition, respectively, and OGLESBY *et al.* (2000a) used the finite-element method with an unstructured mesh. Here we use the boundary integral equation method (BIEM), which is capable of modeling arbitrarily complex fault geometries, although limited to homogeneous unbounded media and an approximate free surface boundary condition. However, the latter approximation is insignificant for the modeling of dynamic effects for blind faults, such as the M 6.7 1994 Northridge earthquake, which was buried 5 km below the surface (OGLESBY *et al.,* 2000a,b; GOTTSCHÄMMER and OLSEN, 2001b).

The importance of modeling the effects of complex fault geometry includes the radiated waves as well as the rupture propagation. In this paper we study the effects of deviation from planar geometries on the resulting ground motion for a buried dipping fault such as the Northridge earthquake. Based on the simulations of spontaneous dynamic rupture propagation, we calculate seismic wave propagation using the finite-difference method (FDM).

## *Fault Models*

We consider three different fault models, as approximations of the 1994 Northridge earthquake, shown in Figure 1. Fault model (B) contains a planar fault with a 40°-dip in agreement with previous seismic inversion models (e.g., WALD *et al.,* 1996), while the remaining two symmetric models (A and C) include faults with 6-km long bends in the upper part. The bends are described by a radius of curvature of 15 km with a maximum change of dip of $\pm 15°$, and have a maximum offset of $\pm 1$ km from the planar part of the fault. In fact, geological and seismological surveys infer a complex fault structure for this earthquake, especially at the upper bound crossing the Santa Susana fault (HUFTILE and YEATS, 1996; MORI *et al.*, 1995; UNRUH *et al.,* 1997; CARENA and SUPPE, 2002). Although the proposed fault models (UNRUH *et al.,* 1997; CARENA and SUPPE, 2002) contain complex geometries both vertically and horizontally, here we examine somewhat simpler models with a single bend toward (model A) and away from (model C) the ground surface, compared to a planar fault model B. The hypocenter is located in the lower right part of the fault, in agreement with that for the Northridge earthquake. The model parameters are summarized in Table 1. Fault dimensions

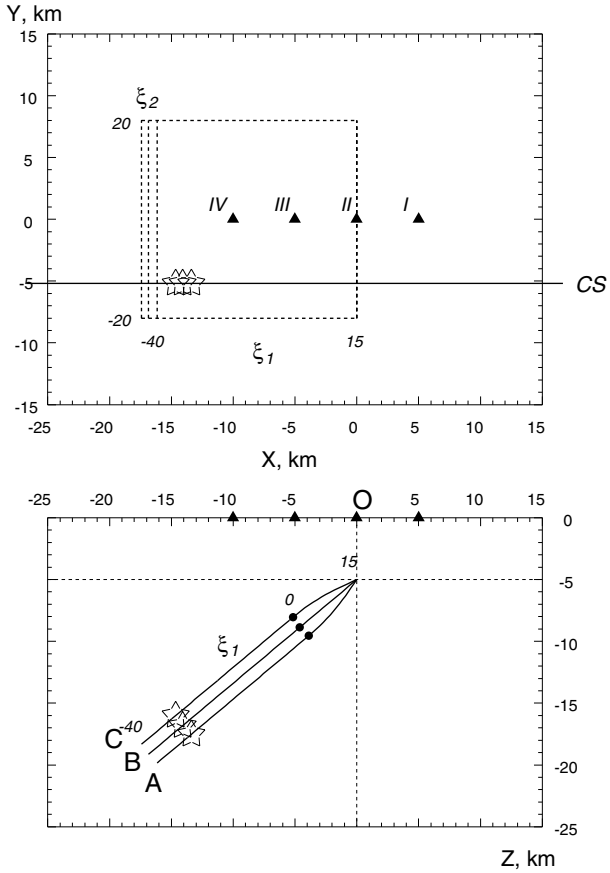


Figure 1
Illustration of the fault models used in our study in map view (top panel) and in a cross section (bottom panel). The stars depict the location of the hypocenters. The numbers along the $\xi_1\xi_2$ axes depict the grid used in the BIEM simulations. Greek numbers depict stations for display of synthetic seismograms. The line CS depicts the position of the cross section used for display of snapshots.

for the three models are 22.4 km $\times$ 16.4 km, regardless of the differences in geometry. For simplicity, we assume a slip rake of 90° in order to examine the effects of a pure thrust fault.

## *Numerical Method*

The first step of our numerical method includes the simulation of spontaneous rupture propagation using a BIEM along a non-planar fault model described above (Aochi *et al.,* 2000a; Tada *et al.,* 2000) in a 3-D homogeneous,

Table 1

*Model parameters used in the numerical simulations*

| |
|---|
| rigidity $\mu$ = 37.0 GPa |
| P-wave velocity $V_p$ = 6.30 [km/s] |
| S-wave velocity $V_s$ = 3.64 [km/s] |
| density $\rho$ = 2800 [kg/m$^3$] |
| grid size in BIEM $\Delta s$ = 400 [m] |
| time step in BIEM $\Delta t$ = 0.032 [sec] |
| fault size ($\xi_1$, $\xi_2$) = (−40:15, −20:20) grid |
| grid size in FDM $\Delta s$ = 400 [m] |
| time step in FDM $\Delta t$ = 0.016 [sec] |
| model region (x, y, z) = (−40:20, −20:20, −30:0) km |

unbounded elastic medium. We do not include any numerical approximation of the free surface, since the depth of burial of the fault (>5 km) is sufficiently large to prevent significant time-dependent normal-stress effects (OGLESBY *et al.,* 2000a,b, NIELSEN and OLSEN, 2000). Rupture is initiated by artificially setting the initial shear stress higher than the peak strength within a circular area of 2 km at the hypocenter.

Step 2 involves inserting the slip history on the fault from step 1 into a FDM simulation (OLSEN *et al.,* 1999). In this procedure, every source time function from the center of the BIEM grids is transformed into a point source in the FD grid, distributed to the neighboring eight nodes weighted according to the distance to conserve the total moment. To avoid high-frequency numerical artifacts in the synthetic ground motions we low-pass filter the source time function (seismic moment) to 1 Hz. The FDM simulation is carried out independently of the BIEM simulation, that is, the wave propagation calculated in the FDM simulation does not affect the source process. The framework of FDM is based on a fourth-order staggered grid (OLSEN, 1994) with the perfectly matched layers (PML) absorbing boundary conditions (COLLINO and TSOGKA, 2001; MARCINKOVICH and OLSEN, 2003) at all boundaries except for the free surface, which is modeled by the zero-stress formulation FS1 described in GOTTSCHÄMMER and OLSEN (2001a). The wave propagation is computed within a region of dimensions 60 km ($x$-axis) $\times$ 40 km ($y$-axis) $\times$ 30 km ($z$-axis, depth).

This procedure is very useful for the case in which the medium surrounding the source region is approximately uniform, far from any boundary or heterogeneity, or for a simple strike-slip fault system with surface rupture in a homogeneous medium (AOCHI and MADARIAGA, 2003). This is a limitation of the formulation of our BIEM. If the material properties at both sides of the fault vary significantly, or if the medium is sufficiently heterogeneous to affect the rupture process, this form of the BIEM cannot be applied directly.

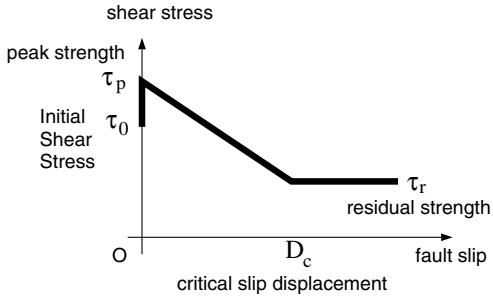


Figure 2
Illustration of the slip-weakening law.

## *Initial Conditions*

The rupture propagation and therefore the radiated waves are strongly dependent on the initial stress and friction law on the fault. We use a simple slip-weakening friction law, where the fault strength $\sigma$ decreases with increasing slip $\Delta u$;

$$\sigma(\Delta u) = \tau_r + \Delta\tau_b(1 - \Delta u/D_c)H(1 - \Delta u/D_c) \tag{1}$$

$$\Delta\tau_b = \tau_p - \tau_r, \tag{2}$$

as illustrated in Figure 2, where $\tau_p$, $\tau_r$ and $\Delta\tau_b$ are the peak strength, the residual strength and the breakdown strength drop, respectively, $D_c$ is the critical slip displacement, and $H(\cdot)$ is the Heaviside function. This relation for shear rupture was originally proposed by Ida (1972) and Palmer and Rice (1973).

For planar fault models, such as those considered in the majority of previous dynamic rupture models, the rupture is controlled by the relative strength drop $\Delta\tau_b$, while the absolute level of strength ($\tau_p$ and $\tau_r$) is arbitrary. However, $\tau_p$ and $\tau_r$ play a significant role on the rupture dynamics especially in non-planar fault models (AOCHI *et al.*, 2000a, 2002; POLIAKOV *et al.,* 2002), dependent on the definition of the frictional parameters and stress field around the fault. In this study we consider two cases described in the following, both using $D_c$ equal to 0.36 m and the breakdown strength drop $\Delta\tau_b$ equal to 10 MPa on the main planar part. The fracture energy using these values is similar to that used by NIELSEN and OLSEN (2000) in their dynamic simulation of the Northridge earthquake. All the parameters are summarized in Table 2.

### *Case 1 (Uniform stress distribution)*

This model assumes constant frictional parameters in Equations (1) and (2), as well as uniform shear and normal stresses everywhere on the fault independent of the fault geometry as illustrated in the left panel of Figure 3. The initial shear and

Table 2

*Initial conditions for the two cases considered in this study. See Figure 4 for the value of $\mu_s$ and $\mu_d$*

| Parameters | Case 1 | Case 2 |
|---|---|---|
| peak strength $\tau_p$ | 10 MPa | $\mu_s \times \sigma_n$ |
| residual strength $\tau_r$ | 0 MPa | $\mu_d \times \sigma_n$ |
| initial shear stress $\tau_0$ | 5 MPa | *driven by* $\sigma_1$ & $\sigma_3$ |
| initial normal stress $\sigma_n^0$ | 0 MPa | *driven by* $\sigma_1$ & $\sigma_3$ |
| critical slip displacement $D_c$ | 0.36 m | 0.36 m |

normal stresses are set to be $\tau_0 = 5$ MPa and $\sigma_n^0 = 0$ MPa, respectively. The model is instructive in quantifying the effects of the fault bend on the stress change, and in particular, on the generation of seismic waves.

*Case 2 (External loading force with Coulomb-Mohr criterion)*

Here we consider an external loading force as illustrated at the right panel in Figure 3 and we introduce a Coulomb-Mohr fracture criterion for the rupture propagation. We assume that the maximum principal stresses $\sigma_1$ and $\sigma_3$ are aligned in the horizontal and vertical directions, respectively ($\Phi = 40°$). We determine the frictional parameters using the Mohr-Coulomb diagram in Figure 4 (top panel). For additional description of the procedure, see AOCHI *et al.* (2002). We define $\tau_p$ and $\tau_r$ as the products of the normal stress $\sigma_n$ and the static/dynamic frictional coefficients ($\mu_s/\mu_d$), respectively. We assume $\mu_s$ to be 0.5. The absolute magnitude of the stress field controls how far the rupture can propagate on a non-planar fault, as demonstrated in AOCHI *et al.* (2000a). If we choose a larger value for $\mu_s$, rupture may be accelerated or decelerated more severely by the fault bends. We select the average of $\sigma_1$ and $\sigma_3$ to be 180 MPa, which corresponds to a depth of 6–7 km at the fault bends. It is possible to introduce a more realistic depth-dependent stress field

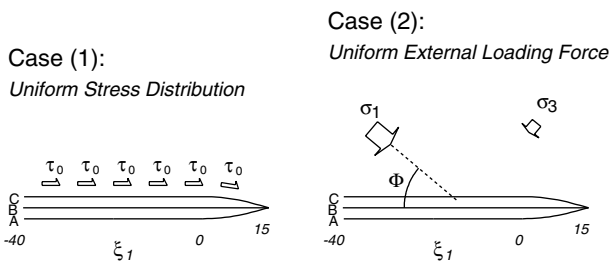


Figure 3

Illustration of the loading system for the fault models. (1) Uniform shear stress $\tau_0$. (2) The stress is loaded by the maximum principal stress $\sigma_1$ with direction $\Phi$ from the main planar part and the minimum principal stress $\sigma_3$.

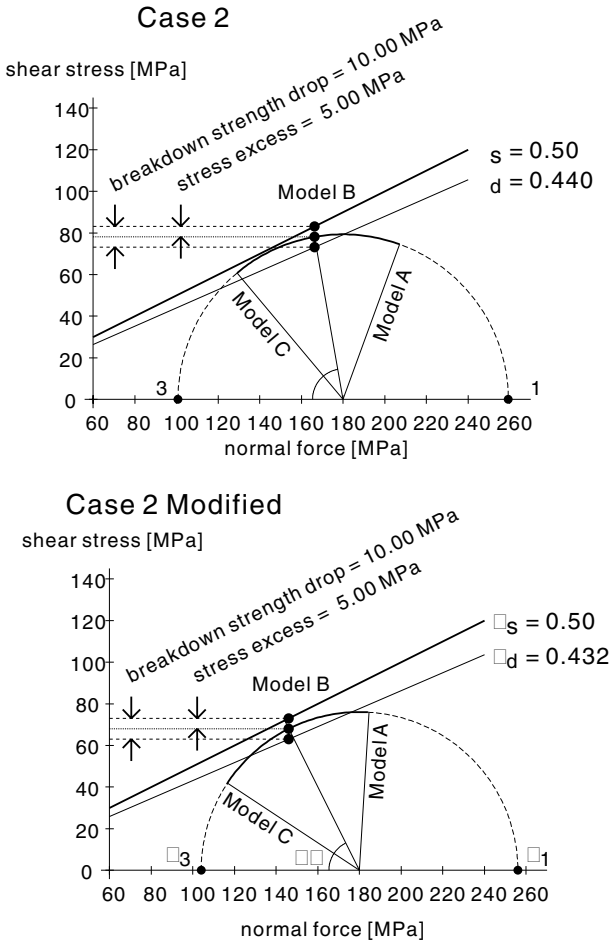


Figure 4
Illustration of the relation between external loading forces ($\sigma_1$ and $\sigma_3$) and the assumed frictional parameters in Case 2. Breakdown strength drop $\Delta\tau_b$ and stress excess ($\tau_p - \tau_0$) are the same on the planar part of each fault model, as indicated by circles of Model B. Initial stress is loaded according to the Mohr circle, clockwise for model A and counterclockwise for model C on the solid curve. (top) Case 2, $\Phi = 40°$, and (bottom) modified Case 2, $\Phi = 31.4°$. The average principal stress $(\sigma_1 + \sigma_3)/2$ and static frictional coefficients $\mu_s$ are constant for both cases.

(Aagaard *et al.*, 2001; Aochi and Madariaga, 2003), even including the pore pressure. Increase in the confining pressure may systematically increase slip amount with depth according to the increase of absolute stress and the resultant stress release. However, for simplicity, we take $\Delta\tau_b$ and stress excess ($\tau_p - \tau_0$) to be 10 MPa and 5 MPa on the planar part which is in the direction of $\Phi = 40°$. These values allow us to analyze the role of the fault bend, since the rupture process is kept constant on the planar part.

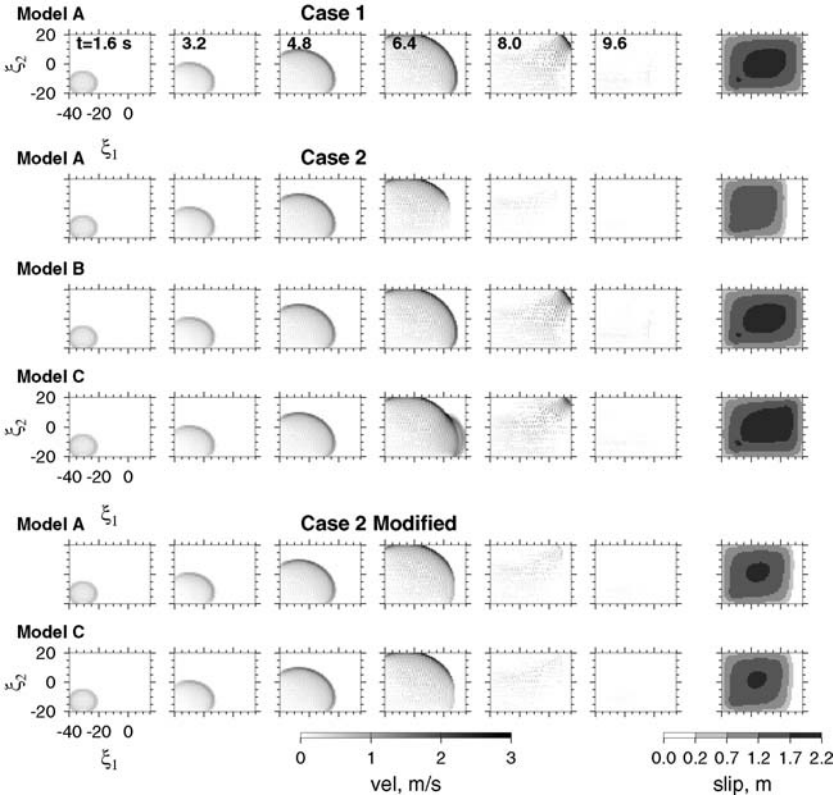


Figure 5
Snapshots of sliprate and final slip distribution (right column) for the different fault models. Top row represents fault model A in Case 1, the 2nd-4th rows represent fault models A, B, and C for Case 2, and the bottom two rows represent fault models A and C for modified Case 2.

## *Simulation Results*

### *Case 1*

Figure 5 (top row) shows rupture propagation for model A in Case 1. The rupture propagates similarly for models A-C both for the planar ($\xi_1 < 0$, $t < 6.4$ s) and non-planar ($\xi_1 > 0$, $t > 6.4$ s) parts of the faults and generates similar final slip distributions corresponding to a seismic moment of 1.76 $\times 10^{19}$ N·m (moment magnitude $M_w$ of 6.76). This is the case since the rupture process is mainly controlled by the significant dynamic change in shear stress accompanied by the rupture front whereas the normal stress change is quite small as shown in Figure 6. Moreover, all fault models impose a constant relation between the stress and frictional parameters ($\Delta\tau_b$, $\tau_p - \tau_0$, $\tau_0 - \tau_r$), implying that the fault bend is sufficiently small not to affect

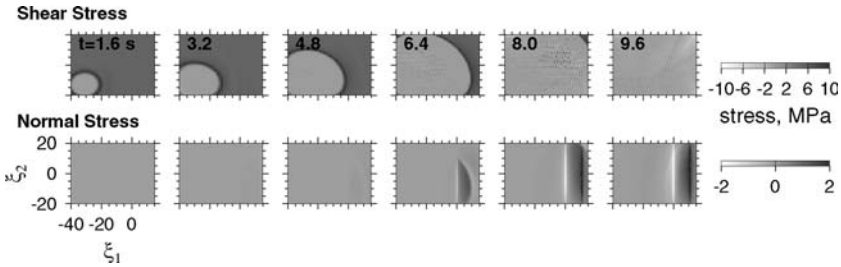


Figure 6
Snapshots of stress propagation on fault model A for Case 1.

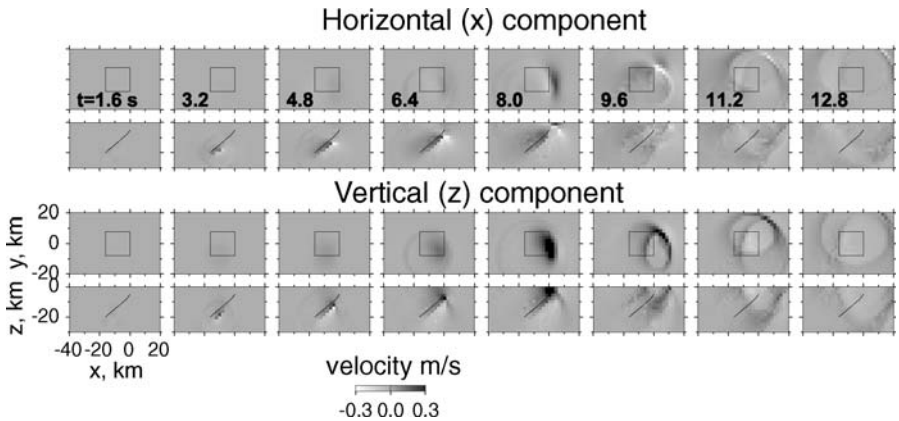


Figure 7
Snapshots of seismic wave propagation in map view (1st and 3rd row) and on a cross section (2nd and 4th row) for fault model A on the strike-perpendicular (top two rows) and vertical (bottom two rows) components.

rupture. Models B and C produce shear stress similar to those for model A (Figure 6), while the normal stress for models A and C is anti-symmetric. Note that shear stress 'overshoots' at the upper right-hand corner due to rupture directivity.

Figure 7 shows simulation results of seismic wave propagation for fault model A. Note the large amplitudes on both horizontal and vertical components, in particular in the forward rupture direction. This directivity effect is also clear in the peak root-mean-square (rms) ground velocity above the fault for all models, shown in Figure 8. The peak velocities show interesting differences due to the fault geometries, despite of constant moment magnitude and similar rupture history. Fault model C generates the largest (bi-modal) and model A the smallest region affected by amplitudes greater than 0.2 m/s, while model A generates the highest peak motions. Compared to the planar fault model B, model A generates increased peak motions up to about 10 km beyond the fault trace in the up-dip direction and generally decreased peak motions

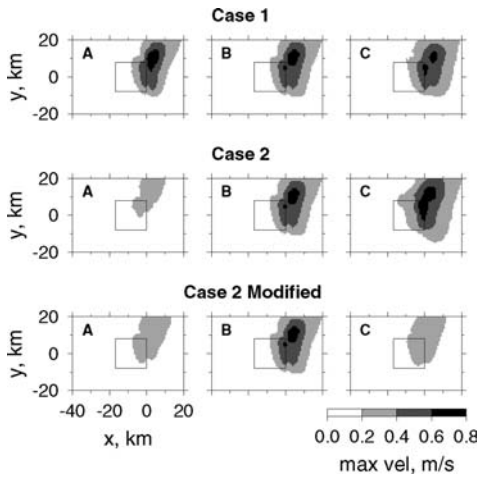


Figure 8
Comparison of maximum rms ground velocity (low-pass filtered up to 1 Hz) for the three fault models. (top row) Case 1, (middle row) Case 2, and (bottom row) modified Case 2.

at further distances. This pattern is reversed for model C. Differences immediately above the fault plane are mainly due to the variation in depth of the planar parts of the faults and therefore less interesting for our analysis.

The seismograms at selected sites in Figure 9 further illustrate the differences in ground motion for models A, B and C. Model A generates the largest peak velocity at station I in the direction of directivity on the strike-perpendicular component ($x$-axis). The peak motions for the three models are similar at stations II (above the fault tip), III and IV (above the fault plane) for the three models. The relatively large amplitudes on the strike-perpendicular IV are due to the relatively closer proximity of the planar part of this model to the surface. Generally, the strike-perpendicular component shows the strongest variation between the models, due to the strong directivity effects in the radiated waves.

*Case 2*

Figure 5 (rows 2–4) shows snapshots on fault models A-C for Case 2. Note that rupture propagation and ground motions for the planar fault (B) are equivalent for cases 1 and 2. However, there are interesting differences in the rupture propagation for models A and C. The fault bend in fault model A causes an earlier arrest of the rupture, while that in model C tends to accelerate the rupture propagation, compared to that for the planar model ($t = 6.4$ s). This difference can be explained from the difference in initial conditions illustrated in Figure 4. The initial stress on the curved part of fault model C is *a priori* closer to the fracture criterion (the part of the circle

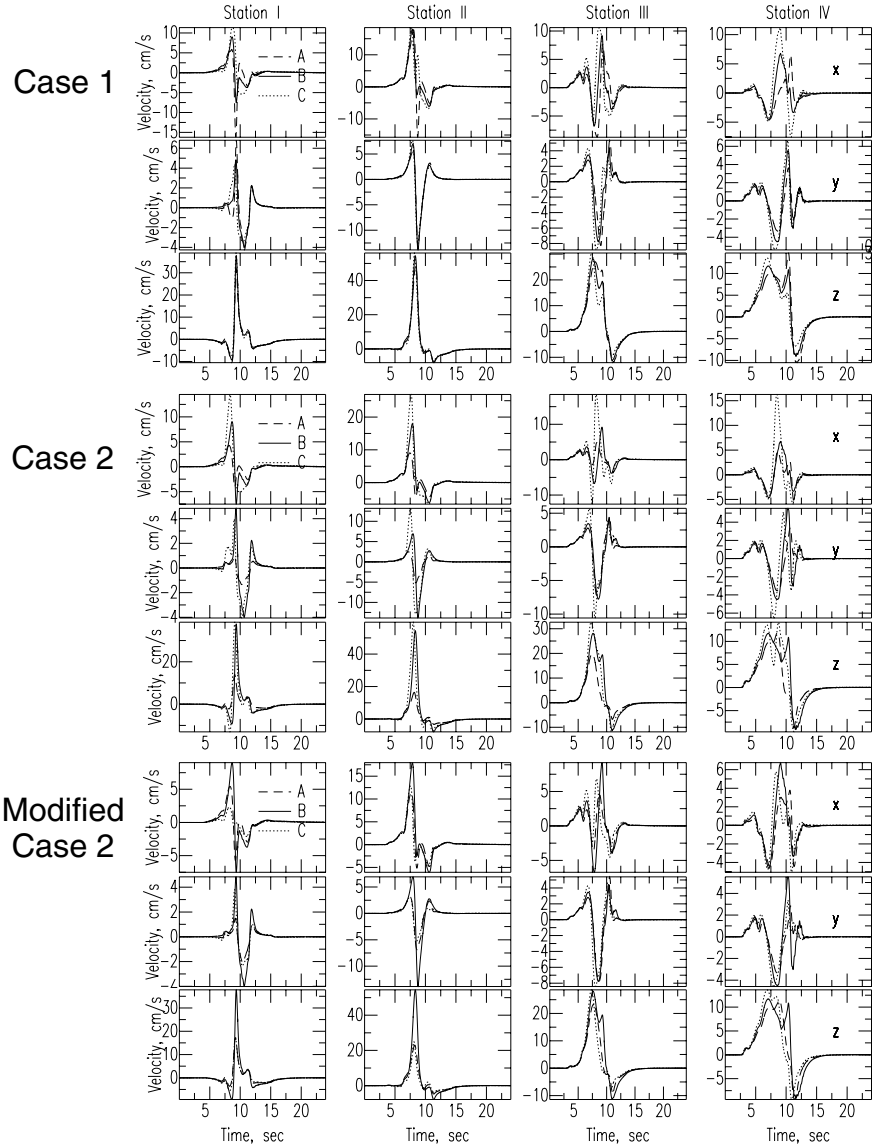


Figure 9
Comparison of synthetic seismograms low-pass filtered up to 1 Hz for the three fault models at four different sites (see Fig. 1 for location). (top) Case 1, (middle) Case 2, and (bottom) modified Case 2.

anticlockwise from the point), while the initial stress field is not favorable for fault model A (clockwise direction). These differences are further illustrated by a slightly larger seismic moment of $1.88 \times 10^{19}$ N·m for model C compared to those for model A ($1.23 \times 10^{19}$ N·m) and for model B ($1.76 \times 10^{19}$ N·m).

The differences in the rupture propagation for the three models discussed above are also evident in the peak motions (Fig. 8) and synthetic seismograms (Fig. 9, middle). Model A generates weaker ground motions due to the earlier arrest of rupture, while the accelerated rupture in model C generates larger-amplitude seismic waves. The synthetic seismograms generally show the largest peak velocities for model C, which on the strike-perpendicular component is up to three times as large as those for models A and B.

These results were obtained assuming horizontal maximum and vertical minimum principal stresses as a loading system. If the principal stresses are aligned in other directions the rupture process will change according to the resulting loading stress on the fault (AOCHI *et al.,* 2002; KAME *et al.,* 2003). To illustrate the effects of the direction of the principal stresses, we simulate an alternative case using $\Phi = 31.7°$ derived from

$$\Phi = \frac{1}{2}\left(\frac{\pi}{2} - \tan^{-1}\mu_s\right), \tag{3}$$

for $\mu_s = 0.5$, as illustrated in Figure 4 (right) and discussed in detail in AOCHI *et al.* (2002). In this case the initial stress on the main planar part is closer to the fracture point than that on the curved parts of the faults, as illustrated in the snapshots of rupture propagation in Figure 5 (bottom). For both models A and C, rupture is arrested around the curved parts of the faults in models A and C, in contrast to the situation for model B. The seismograms in Figure 9 (bottom) differ significantly from those in cases 1 and 2. The peak motions are generally largest for model B, and the differences are significant for all components near the tip of the fault as well as in the forward rupture direction. The differences are smaller immediately above the fault plane.

## *Conclusions*

Our results suggest that slight differences in the curvature of the upper part of a buried thrust fault can significantly affect the rupture dynamics, mainly due to differences in the assumed initial conditions. For a uniform stress distribution and uniform frictional properties, the variation in fault geometry in our models generates similar rupture history with relatively small and localized differences in ground motion, due to variation in directivity from the curved parts of the faults. However, if a Coulomb type friction law and an external loading force control the fault properties, the rupture propagation and the radiated waves change significantly due to the fault curvature. In this case, the direction of the external loading force becomes very important, affecting acceleration, deceleration and/or arrest of rupture as observed in a branched fault system (AOCHI *et al.,* 2002; KAME *et al.,* 2003). In other words, the rupture process depends on the most favorable direction

of the fault with respect to the external stress field. The differences in the rupture process also affect the near-field seismograms and the peak velocities by up to a factor of 2–3 near the fault. Our results imply that the dynamic rupture process must be modeled carefully based on a reasonable fault geometry and loading force in order to obtain accurate near-field ground motion estimates and even for long-period waves.

*Acknowledgements*

This research was supported by NSF (EAR-0003275) and the Southern California Earthquake Center. SCEC is funded by NSF Cooperative Agreement EAR-0106924 and USGS Cooperative Agreement 02HQAG0008. The SCEC contribution number for this paper is 721, and the ICS contribution number is 555. The BIEM and FDM calculations were carried out on parallel computers at Pittsburgh Supercomputing Center (Compaq Alphaserver Cluster), NSF Award EAR-020001P, and at Information Services Division, University of Southern California (IBM Netfinity Cluster).

## References

Aagaard, B. T., Heaton, T. H., and Hall, J. F. (2001) *Dynamic Earthquake Rupture in the Presence of Lithostatic Normal Stress: Implication for Friction Models and Heat Production*, Bull. Seismoc. Soc. Am. *91*, 1763–1796.

Aochi, H., Fukuyama E., and Matsu'ura, M. (2000a), *Spontaneous Rupture Propagation on a Non-planar Fault in 3-D Elastic Medium*, *157*, 2003–2027.

Aochi, H., Fukuyama, E., and Matsu'ura, M. (2000b) *Selectivity of Spontaneous Rupture Propagation on a Branched Fault*, Geophys. Res. Lett. *27*, 3635–3638.

Aochi, H. and Madariaga, R. (2003) *The 1999 Izmit, Turkey, Earthquake: Non-planar Fault Structure, Dynamic Rupture Process and Strong Ground Motion*, Bull. Seismoc. Soc. Am. *93*, 1249–1266.

Aochi, H., Madariaga, R., and Fukuyama E. (2002) *Effect of Normal Stress during Rupture Propagation Along Non-planar Fault*, J. Geophys. Res. *107*(B2), ESE 4, 1–12.

Carena, S. and Suppe, J. (2002) *3-D Imaging of Active Structures Using Earthquake Aftershocks: The Northridge Thrust, California*, J. Structural Geology *24*, 887–904, 2002.

Collino, F. and Tsogka, C. (2001) *Application of the Perfectly Matched Absorbing Layer Model to the Linear Elastodynamic Problem in Anisotropic Heterogeneous Media*, Geophysics *66*, 294–307.

Gottschämmer, E. and Olsen, K. B. (2001a) *Accuracy of the Explicit Planar Free-surface Boundary Condition Implemented in a Fourth-order Staggered-grid Velocity-stress Finite-difference Scheme*, Bull. Seismoc. Soc. Am. *91*, 617–623.

Gottschämmer, E. and Olsen, K. B. (2001b) *Ground Motion Synthetics for Spontaneous versus Prescribed Rupture on a 45 Thrust Fault*, EOS Trans, AGU, *82*(47), Fall Meet. Suppl. Abstract S42C-0667.

Harris, R. A. and Day, S. M. (1993) *Dynamics of Fault Interaction: Parallel Strike-slip Faults*, J. Geophys. Res. *98*, 4461–4472.

Harris, R. A. and Day, S. M. (1999) *Dynamic 3-D Simulations of Earthquakes on en echelon Faults*, Geophys. Res. Lett. *26*, 2089–2092.

HUFTILE, G. J. and YEATS, R. S. (1996) *Deformation Rates across the Placerita (Northridge $M_w$ = 6.7 Aftershock Zone) and Hopper Canyon Segments of the Western Transverse Ranges Deformation Belt*, Bull. Seismoc. Soc. Am. *86*, S3–S18.

IDA, Y. (1972) *Cohesive Force across the Tip of a Longitudinal-shear Crack and Griffith's Specific Surface Energy*, J. Geophys. Res. *77*, 3796–3805.

KAME, N., RICE, J. R., and DMOWSKA, R. (2003) *Effects of Prestress State and Rupture Velocity on Dynamic Fault Branching*, J. Geophys. Res. 108(B5), 2265, doi: 10.1029/2002JB002189.

KAME, N. and YAMASHITA, T. (1997) *Dynamic Nucleation Process of Shallow Earthquake Faulting in a Fault zone*, Geophys. J. Int. *128*, 204–216.

K*ame*, N. and YAMASHITA, T. (1999) *Simulation of the Spontaneous Growth of a Dynamic Crack without Constraints on the Crack Tip Path*, Geophys. J. Int. *139*, 345–358.

KASE, Y. and KUGE, K. (1998) *Numerical Simulation of Spontaneous Rupture Processes on Two Non-coplanar Faults: The Effect of Geometry on Fault Interaction*, Geophys. J. Int. *135*, 911–922.

KING, G. and NÁBĚLEK, J. (1985) *Role of Fault Bends in the Initiation and Termination of Earthquake Rupture*, Science *228*, 984–987.

MARCINKOVICH, C. and OLSEN, K.B. (2003) *On the Implementation of Perfectly Matched Layers in a 3-D Fourth-order Velocity-stress Finite-difference Scheme*, J. Geophys. Res. 2002JB002235.

MIKUMO, T. and MIYATAKE, T. (1993) *Dynamic Rupture Processes on a Dipping Fault, and Estimates of Stress Drop and Strength Excess from the Results of Waveform Inversion*, Geophys. J. Int. *112*, 481–496.

MORI, J., WALD, D. J., and WESSON, R. L. (1995) *Overlapping Fault Planes of the 1971 San Fernando and 1994 Northridge, California Earthquake*, Geophys. Res. Lett. *22*, 1033–1036.

NIELSEN, S. and OLSEN, K. B. (2000) *Constraints on Stress and Friction from Dynamic Rupture Models of the 1994 Northridge, California, Earthquake*, *157*, 2029–2046.

OGLESBY, D. D. and ARCHULETA, R. J. (2003) *The Three-dimensional Dynamics of a Non-planar Thrust Fault*, Bull. Seismoc. Soc. Am. *93*, 2222–2235.

OGLESBY, D. D., ARCHULETA, R. J., and NIELSEN, S. B. (2000a) *The Three-dimensional Dynamics of Dipping Faults*, Bull. Seismoc. Soc. Am. *90*, 616–628.

OGLESBY, D. D., ARCHULETA, R. J., and NIELSEN, S. B. (2000b) *Dynamics of Dip-slip Faulting: Explorations in Two Dimensions*, J. Geophys. Res. *105*, 13643–13653.

OGLESBY, D. D., DAY, S. M., LI, Y., and VIDALE, J. E. (2001) *The 1999 Hector Mine Earthquake: The Dynamics of a Branched Fault*, EOS Trans. AGU, 82(47), Fall Meet. Suppl., Abstract S11C-05.

OLSEN, K. B. (1994) *Simulation of Three-dimensional Wave Propagation in the Salt Lake Basin*, Ph.D. Thesis, University of Utah.

OLSEN, K. B., FUKUYAMA, E., AOCHI, H. and MADARIAGA, R. (1999) *Hybrid Modeling of Curved Fault Radiation in a 3D Heterogeneous Medium, 2nd ACES Workshop Proceedings* (ed. M. Matsu'ura, K. Nakajima and P. Mora) pp 343–349.

PALMER, A. C. and RICE, J. R. (1973) *The Growth of Slip Surfaces in the Progressive Failure of Overconsolidated Clay*, Proc. Roy. Soc. Lond. A *332*, 527–548.

POLIAKOV, A. N. B., DMOWSKA, R., and RICE, J. R. (2002) *Dynamic Shear Rupture Interactions with Fault Bends and Off-axis Secondary Faulting,* J. Geophys. Res. *107*(B11), ESE 6, 1–18.

SIBSON, R. H. (1986) *Rupture interaction with fault jogs, In Earthquake Source Mechanics*, AGU Geophys. Mono., 37 (ed. S. Das, J. Boatwright and C. H. Scholz), (American Geophysical Union, Washington D. C.) pp 157–167.

TADA, T. and YAMASHITA, T. (1996) *The Paradox of Smooth and Abrupt Bends in Two-dimensional In-plane Shear-crack Mechanics*, Geophys. J. Int. *127*, 795–800.

TADA, T. and YAMASHITA, T. (1997) *Non-hypersingular Boundary Integral Equations for Two-dimensional Non-planar Crack Analysis*, Geophys. J. Int. *130*, 269–282.

TADA, T., FUKUYAMA, E. and MADARIAGA, R. (2000) *Non-hypersingular Boundary Integral Equations for 3-D Non-planar Crack Dynamics*, Comp. Mech. *25*, 613–626.

UNRUH, J. R., TWISS, R. J., and HAUKSSON, E. (1997) *Kinematics of Postseismic Relaxation from Aftershock Focal Mechanisms of the 1994 Northridge, California, Earthquake,* J. Geophys. Res. *102*, 24,589–24,603.

WALD, D. J., HEATON, T. H., and HUDNUT, K. W. (1996) *The Slip History of the 1994 Northridge, California, Earthquake Determined from Strong-motion, Teleseismic, GPS, and Leveling Data*, Bull. Seismoc. Soc. Am. *86*, S49–S70.

(Received 27 September 2002, revised April 25, 2003, accepted May 5, 2003)

To access this journal online:
http://www.birkhauser.ch